Co-design of zinc titanium nitride semiconductor towards durable photoelectrochemical applications

Ann L. Greenaway[1]*, Sijia Ke[2,3], Theodore Culman[1], Kevin R. Talley[1], John S. Mangum[1], Karen N. Heinselman[1], Ryan S. Kingsbury[4], Rebecca W. Smaha[1], Elisa M. Miller[1], Kristin A. Persson[3,5], John M. Gregoire[6], Sage R. Bauers[1], Jeffrey B. Neaton[2,7,8], Adele C. Tamboli[1,9], Andriy Zakutayev[1]*

[1] Materials Chemical and Computational Science Directorate, National Renewable Energy Laboratory, Golden, CO 80401, USA
[2] Materials and Chemical Sciences Division, Lawrence Berkeley National Laboratory, Berkeley, CA 94720, USA
[3] Department of Materials Science and Engineering, University of California Berkeley, Berkeley, CA 94720, USA
[4] Energy Storage and Distributed Resources Division, Lawrence Berkeley National Laboratory, Berkeley, California 94720, USA
[5] Molecular Foundry, Lawrence Berkeley National Laboratory, Berkeley, California 94720, USA
[6] Division of Engineering and Applied Science, California Institute of Technology, Pasadena, CA 91125, USA
[7] Department of Physics, University of California Berkeley, Berkeley, CA 94720, USA
[8] Kavli Energy Nanosciences Institute at Berkeley, Berkeley, CA 94720, USA
[9] Department of Physics, Colorado School of Mines, Golden, Colorado 80401, USA

*Corresponding authors: Ann.Greenaway@nrel.gov, Andriy.Zakutayev@nrel.gov

Abstract
Photoelectrochemical fuel generation is a promising route to sustainable liquid fuels produced from water and captured carbon dioxide with sunlight as the energy input. Development of such technologies requires photoelectrode materials that are both photocatalytically active and operationally stable in harsh oxidative and/or reductive electrochemical environments. Such photocatalysts can be discovered based on co-design principles, wherein design for stability is based on the propensity for the photocatalyst to self-passivate under operating conditions and design for photoactivity is based on the ability to integrate the photocatalyst with established semiconductor substrates. Here we report on synthesis and characterization of zinc titanium nitride ($ZnTiN_2$) that follows these design rules by having a wurtzite-derived crystal structure and showing self-passivating surface oxides created by electrochemical polarization. The sputtered $ZnTiN_2$ thin films have optical absorption onsets below 2 eV and n-type electrical conduction of 0.1 S/cm. The band gap of this material is reduced from the 3.5 eV theoretical value by cation site disorder, and the impact of cation antisites on the band structure of $ZnTiN_2$ is explored using density functional theory. Under electrochemical polarization, the $ZnTiN_2$ surfaces have TiO_2- or ZnO-like character, consistent with Materials Project Pourbaix calculations predicting the formation of stable solid phases under near-neutral pH. These results show that $ZnTiN_2$ is a promising candidate for photoelectrochemical liquid fuel generation and demonstrate a new materials design approach to other photoelectrodes with self-passivating native operational surface chemistry.

Broader Impact

Photoelectrochemical fuel generation has been stymied by a lack of photoelectrode materials which are both highly active and stable under long-term operation. Searches for new photoelectrodes have typically selected either stability or activity, with the intent to improve the other characteristic after the fact. Inspired by technologies that employ designed surface transformations for operational stability, such as the precipitation strengthening of Ni-based superalloys in gas turbines, here we employ co-design principles to identify a candidate photoelectrode material which can fill both stability and activity requirements. We synthesize this promising candidate photoelectrode material, $ZnTiN_2$, which forms stable protective oxides under electrochemical operation, providing a route to stability, while being structurally compatible with established semiconductors, enabling good optoelectronic properties. We investigate the optoelectronic properties and electrochemical stability of $ZnTiN_2$ both experimentally and computationally. These results confirm the promise of $ZnTiN_2$ as a photoelectrode material and point to a successful new materials design strategy for photoelectrode development.

1. Introduction

Photoelectrochemical carbon dioxide reduction (PEC CO_2R) is a promising route to recycling captured CO_2 in the form of liquid chemical fuels using sunlight as the energy input. Practical PEC CO_2R systems will require the development of multiple components, including high-performing catalysts,[1] separation membranes,[2] and coupled microenvironments,[3,4] as well as the integration and scale-up of these materials and processes.[5] A critical factor for the future success of PEC CO_2R is the identification of suitable photoelectrode materials to convert photons to electrons to drive CO_2R as well as the oxygen evolution reaction (OER) that enables the production of fuel using only CO_2 and H_2O as reactants.[6,7] Like semiconductors used in photovoltaics, these photoabsorbers are subject to stringent requirements of strong absorptivity, long carrier lifetimes, and appropriate band gap, but with the added constraints of band edge positions that can drive the reaction of interest, suitable adsorption/desorption kinetics at the surface, and, critically, operational stability in aqueous environments.[6,8]

Photocatalyst discovery campaigns have focused on down-selecting from a broad range of candidate materials based on thermodynamic and electronic structure criteria, with great success in identifying photocatalysts that meet some but not all performance requirements.[6,9–11] The primary challenge framed by prior work is the simultaneous realization of long-term operational stability and high radiative efficiency. This grand challenge can be addressed by a co-design approach, wherein photocatalyst design originates from device-level experiential knowledge. Recent implementations in other technologies have demonstrated the value of co-design for solving challenging multi-objective problems.[12,13] In the present case, we design photocatalysts based on experience from photoelectrochemical and photovoltaic devices. From photoelectrochemical devices, we embrace electrochemical self-passivation, focusing on kinetic (as opposed to thermodynamic) operational stabilization. From photovoltaics, we recognize that synthetic control of defects is paramount to rapid translation from materials discovery to high efficiency devices, and that heteroepitaxial growth on established semiconductor substrates is a demonstrated method to enable high efficiency absorbers. A key attribute of co-design is disruption of the sequential design process, which for photocatalysts has traditionally been materials discovery based on performance criteria followed by synthesis for device implementation. Co-design ensures that integration and scale-up process accompanies each

discovered photocatalyst, a transformational research approach that can amplify the impact of discovery science.[14]

While the most-investigated photovoltaic materials (Si, III-Vs, and II-VI compounds) have promising properties for PEC applications, all corrode rapidly under electrochemical operation, a result of their low Pourbaix stability.[7,15–17] Substantial efforts have been dedicated to limiting such corrosion,[18,19] but these have failed to generate photoelectrodes with surfaces which are durable for more than tens of hours of operation. While these issues can be partially addressed via application of a protection layer, such approaches are undesirable due to complex processing[20] and the propensity for degradation from electrolyte infiltration at pinholes or grain boundaries.[15] The lesson from prior device implementations is that even with protective coatings, the semiconductor light absorber must self-passivate under operating conditions. Though metal oxides have been a common target of photoanode searches due in part to their relatively small driving force for corrosion compared to traditional photovoltaic semiconductors,[9–11] the most prolific solar energy converter, $BiVO_4$, suffers from its lack of self-passivation,[21,22] and new classes of self-passivating oxides such as copper vanadates[23] suffer from poor carrier transport. Searches beyond metal oxides have identified promising candidates that do self-passivate, such as Ta_3N_5[24–26] and Sb_2S_3,[27–29] but further development has been hampered by the inability to effectively integrate these semiconductors into high efficiency photoelectrochemical generators.

In photoelectrode co-design, it is critical to consider materials that could be paired with established semiconductors to impart good material quality *via* heteroepitaxy and have surfaces that transform under operation in aqueous conditions to stable coatings with compatible crystal structures. Recent work in computational materials discovery has predicted a trove of nitride semiconductors with earth-abundant constituent elements that merit evaluation against these criteria.[30,31] A family of Zn- or Mg-based multivalent ternaries with crystal structures derived from wurtzite or rocksalt parent compounds[32,33] is particularly promising; these nitrides can be integrated with wide-bandgap GaN and related III-N wurtzite semiconductors that are amenable to p-type doping for contact formation. Examples of the experimentally synthesized wurtzite materials in this family include Zn_2VN_3,[34] $MgSnN_2$,[35,36] Zn_2NbN_3,[37] Zn_3MoN_4,[38] Zn_2SbN_3,[39] Mg_2SbN_3,[40] Mg_2PN_3 and Zn_2PN_3,[41,42] among others. For several well-studied materials in this family, such as wurtzite $ZnSnN_2$[43,44] and $ZnGeN_2$[45–47] as well as rocksalt Mg_2NbN_3[48] and $MgZrN_2$,[49–51] elemental disorder on cation sublattice of the parent structure has been shown to influence both band gap and transport properties,[45,52] although this phenomenon has not been studied across the broader class.[52–54] However, none of the above multivalent ternary nitrides have been considered for PEC applications, with research in this space limited to wurtzite oxynitride alloys such as $ZnGeN_2$-ZnO[55] or $ZnSnN_2$-ZnO,[56] despite the potential for integration with GaN (or other III-N),[57,58] and many other theoretical predictions have never been synthesized so their experimental properties remain unknown.

One particularly suitable candidate material in this chemical and structural space is $ZnTiN_2$, which has not previously been synthesized. This material has been theoretically predicted to be stable with a cation-ordered wurtzite-derived crystal structure compatible with wurtzite GaN,[59] with other independent computational studies supporting these theoretical predictions.[30,31] Materials Project Pourbaix stability calculations[7,60–62] indicate that $ZnTiN_2$ will decompose to stable oxides such as ZnO and TiO_2 in near-neutral pH aqueous environments. These ZnO and TiO_2 decomposition products are not only electrochemically stable under the operating conditions, but are also utilized in other applications as transparent conducting oxides with good electrical charge transport and wide optical band gaps. In addition, TiO_2 has been

extensively studied as an archetype photoelectrochemical fuel generation material with exceptional stability,[7] and as a stabilizing coating layer with suitable charge transport properties on high-quality Si and III-V photovoltaic absorbers used in photoelectrochemical applications.[19] All these theoretical predictions and scientific hypotheses together call for experimental investigations of $ZnTiN_2$.

Here we report on the synthesis and characterization of zinc titanium nitride ($ZnTiN_2$) and evaluate its chemical and physical properties toward photoelectrochemical applications. The sputtered thin films crystallize in cation-disordered wurtzite-derived structure with strong (002) preferential orientation normal to the substrate surface, in a composition window from stoichiometric $ZnTiN_2$ up to ~60% Zn on the cation site, and with unintentional oxygen incorporation of less than 10 anion % in the bulk of the layers. The $ZnTiN_2$ films show an optical absorption onset close to 2 eV and n-type transport with high electron doping indicated by 0.3 Ω-cm electrical resistivity and S = -50 μV K^{-1} Seebeck coefficient. Density functional theory (DFT) calculations show that this reduced band gap compared to the predicted 3.5 eV[31] value may be due to band shifts caused by non-stoichiometric N-centered Zn_1Ti_3 and Zn_3Ti_1 tetrahedral motifs in cation-disordered $ZnTiN_2$, the presence of which broaden the band structure near the band edges, reducing the gap. $ZnTiN_2$ electrodes show ZnO-like or TiO_2-like character depending on the pH operating conditions and regardless of the applied potential near CO_2R and OER operating conditions. These results show that the $ZnTiN_2$ wurtzite semiconductor may have bulk optoelectronic properties and self-passivating surface chemistry suitable for photoelectrochemical fuel generation and point to a new material design strategy for photoelectrode development.

2. Results and Discussion

2.1 Crystal structure and phase competition

Synthesis of $ZnTiN_2$ films was carried out using radio-frequency reactive co-sputtering (see Methods). Fig.1 shows the results of x-ray diffraction (XRD) measurements of $ZnTiN_2$ thin films with varying cation composition, Zn/(Zn+Ti), measured by x-ray fluorescence (XRF). The XRD patterns of these polycrystalline samples deposited at ambient temperature on Si substrates have the strongest peak at 2θ = 36°, as well as several weaker reflections. As shown in Fig.1a for the $ZnTiN_2$ sample with Zn/(Zn+Ti) = 0.5, this main peak can be attributed to the (002) wurtzite (WZ) reflection, as supported by the (100) peak at 33°, (101) peak at 38° and (102) peak at 49°. Computational work predicts an orthorhombic structure ($Pna2_1$, space group 33) for cation-ordered $ZnTiN_2$;[30,31,59] like other ternary nitrides of this type,[35,44,47,52] $ZnTiN_2$ experimentally takes a cation-disordered, wurtzite-type structure. The absence of low-angle reflections (between 20 and 25° 2θ) and high-angle peak splitting are indicative of the long-range cation disorder in this material.[52] Assuming an orthorhombic unit cell, the lattice constants deduced from the experimental peak positions are a = 5.4 Å, b = 6.2 Å, c = 5.0 Å; for a wurtzite-type structure, the lattice constants would be a = 3.1 Å and c = 5.0 Å (CIF files included in SI). The strong intensity of the (002) peak indicates that the $ZnTiN_2$ films have strong c-axis preferential orientation, which has been reported for other ternary nitrides with a wurtzite-derived crystal structure.[44,47]
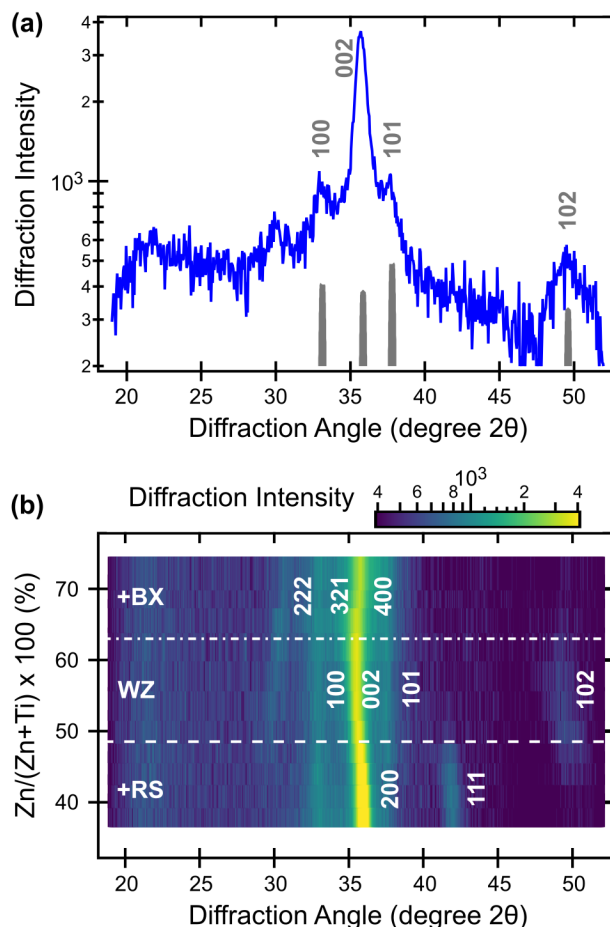
Fig.1 X-ray diffraction (XRD, Cu Kα radiation) of polycrystalline ZnTiN$_2$ thin films. (a) Diffraction from a near-stoichiometric (Zn/(Zn+Ti) = 0.5) polycrystalline film, with an experiment-modeled disordered ZnTiN$_2$ diffraction pattern (grey, refer to description in text). (b) Composition-dependent XRD heat map illustrating the presence of other phases at low (RS) and high (BX) Zn/(Zn+Ti).

The WZ-derived structure is stable from 0.5 < Zn/(Zn+Ti) < 0.6, where the high-angle WZ (102) peak at 49° coexists with a minor seconday phase with a peak at 30°, as shown in Fig.1b. For the Ti-rich (Zn-poor) compositions of Zn/(Zn+Ti) < 0.5, there is a clear secondary rocksalt-derived (RS) phase, likely TiN, indicated by the (111) peak at 42°, as well as strengthening and a clear shift of the highest intensity peak towards higher angle to become RS TiN (200). For the Zn-rich (Ti-poor) compositions, Zn/(Zn+Ti) > 0.5, there is a secondary fluorite-derived phase, likely anti-bixbyite (BX) Zn$_3$N$_2$; this assignment is supported by the (222) reflection at 30° accompanied by a small shift of the main (400) peak to a higher angle. Annealing these materials in N$_2$ atmosphere did not substantially change the crystallinity or phase content up to 500-600 °C and led to rapid Zn, N, and thickness loss at and above 700 °C (see Figure S1 in SI). The finite composition width of the WZ phase space, as well as the competition with the RS phase (on the Zn-poor side) and BX phase (on the Zn-rich side), are similar to what has been reported for other zinc transition metal nitrides.[34,63]

The experimental observation of ZnTiN$_2$ with a WZ-derived structure (Fig. 1a) and its competing RS and BX phases (Fig.1b) are generally consistent with the previously published theoretical predictions for crystal structure and thermodynamic stability of this material. Fig. 2

shows the convex hull stability diagrams for the full Zn-Ti-N ternary space (Fig. 2a) and along a pseudo-binary (Zn_3N_2)-($TiN+N_2$) tie-line (Fig. 2b), adapted from Ref. [30]. According to these DFT calculations, the main competing phases of $ZnTiN_2$ are Zn_3N_2 on the Zn-rich side and TiN on Ti-rich side of the ternary composition, in agreement with our experimental measurements (Fig. 1b). The calculated formation enthalpy of $ZnTiN_2$ from the elements was -1.154 eV/atom, and its decomposition energy into the competing Zn_3N_2 and TiN phases was +0.035 eV/atom,[30] indicating $ZnTiN_2$ is a thermodynamically stable material. It is important to note that these theoretical predictions were made for cation-ordered $ZnTiN_2$, whereas experimental measurements do not show evidence of such long-range ordering (Fig. 1). However, as shown below (Section 2.4), the computed energy to interchange Zn and Ti atoms in $ZnTiN_2$, introducing antisite defects and off-stoichiometric motifs that reduce the band gap, can be as small as ~0.01 eV/atom depending on concentration and the specific configuration. This is significantly smaller than the calculated formation enthalpies or decomposition energies discussed here.
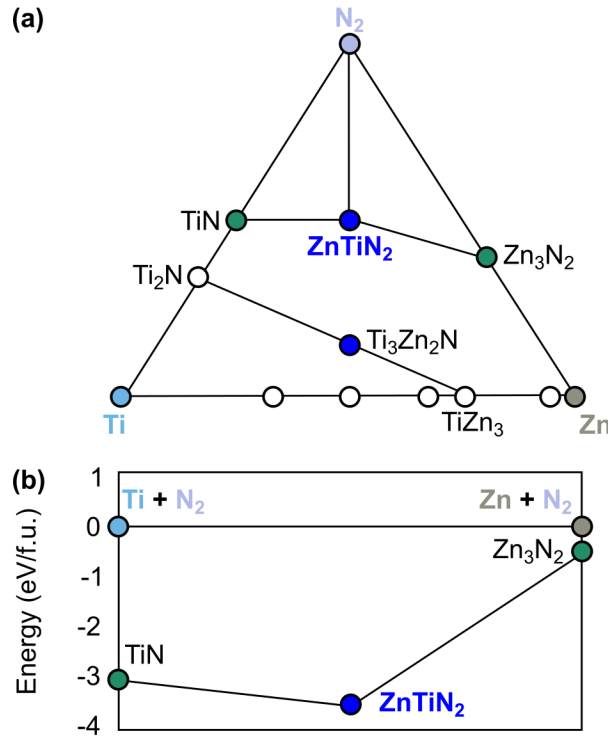

Fig.2 Calculated thermochemical stability of $ZnTiN_2$ (a) 3D convex hull adapted from Ref [30]. (b) 2D convex hull projection based on calculations from the NRELMatDB, ref [64], consistent with the calculations in Ref [30]. Blue circles represent stable ternary materials and green circles represent stable binary compounds; white circles are unstable compounds. Elemental reference states are given with associated colors.

2.2. Synthetic control of crystallinity in (002)-oriented films

Rutherford backscattering spectrometry (RBS) data were acquired from a film with $Zn/(Zn+Ti) \approx 0.5$ as measured by XRF (Fig. 3a). A two-layer model of the Si substrate and the $ZnTiN_2$ film constrained to equal numbers of cations and anions indicates equal amounts of Zn and Ti, in agreement with XRF. The RBS data also show the presence of oxygen, approximately 10% of the total anion composition, O/(N+O). Some fraction of this oxygen is likely due to oxidation of films after removal from the deposition chamber. Fig. 3b compares the bulk

composition of the film (from RBS) with the surface composition (from x-ray photoelectron spectroscopy, XPS,), which shows that the film is heavily oxidized and substantially Zn-rich at the surface. A negative Seebeck coefficient measured from these films (discussed later) does, however, suggest the incorporation of some *n*-type O impurities on N sites (O_N) in the film.
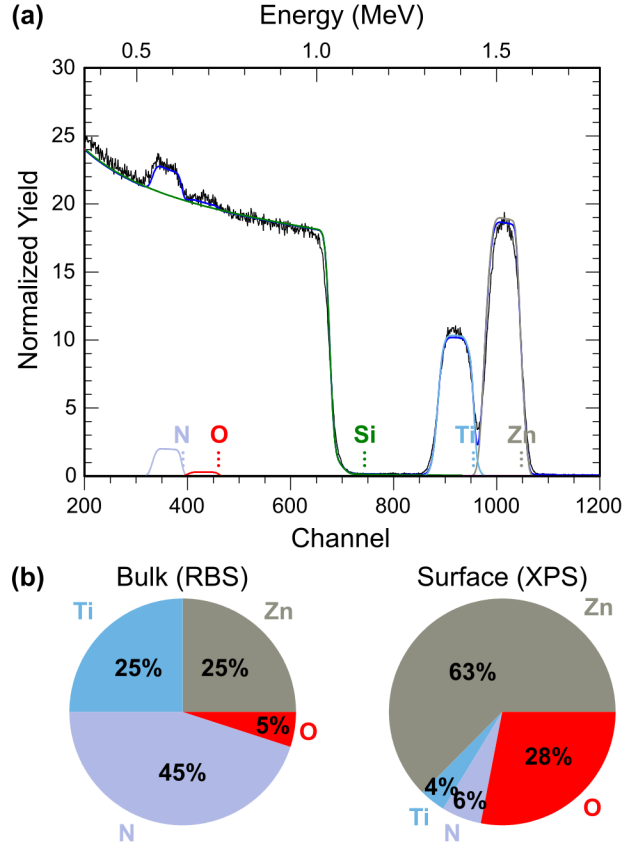

Fig. 3 Composition of $ZnTiN_2$ thin films. (a) Representative RBS spectrum showing contributions from Zn, Ti, N, O, and the substrate (Si). The overall fit is shown as a solid blue line. (b) Pie charts comparing bulk (RBS, from (a)) and surface (top ~10 nm, XPS) compositions of representative films.

To improve the crystallinity of the $ZnTiN_2$ material and study its optical and electrical properties, highly textured (002)-oriented films were grown by RF co-sputtering directly onto heated EXG glass substrates by a single-step deposition process (complete deposition conditions are given in Table S1). Factors influencing crystallinity were studied by tracking the position and amplitude of the diffraction reflection around $2\theta = 36°$ as a function of composition and deposition temperature (Fig 4a). The cation composition of the films ranged from $0.05 <$ Zn/(Zn+Ti) < 0.91 and was primarily controlled by modifying the relative powers of the Ti and Zn sputtering targets. Less Zn incorporation was observed as the deposition temperature set point (for films with temperature gradients, described in the Methods) was increased from 175 °C to 310 °C while keeping the target powers constant, due to the higher volatility of Zn compared to Ti. Around $0.5 <$ Zn/(Zn+Ti) < 0.6, the peak amplitude is maximized. The peak center is closest to that of the (002) reflection of the wurtzite $ZnTiN_2$ structure at slightly higher Zn compositions, $0.6 <$ Zn/(Zn+Ti) < 0.65. As the film cation composition becomes either Ti-rich or Zn-rich, the peak amplitude decreases and the peak center shifts to higher 2θ, consistent with the additional

phases observed in Fig.1b. For films with near-stoichiometric cation compositions, Zn/(Zn+Ti) = 0.5, a single reflection, shown in Fig. 4b, is observed in 2D X-ray diffraction centered around χ = 90° and $2\theta \approx 36°$, corresponding to the (002) reflection of WZ ZnTiN$_2$. The spread in χ from approximately 70° to 110° clearly displays the textured nature of the films, in agreement with the tilted columnar microstructure observed by cross-sectional SEM (Fig. 4c). The nominal film thickness, measured by SEM, is ~150 nm. Most of the textured columnar microstructure exhibits grain sizes ranging from 20–30 nm in the horizontal in-plane direction and 50–150 nm in the vertical growth direction. However, in the first 20 nm of growth, the microstructure consists of much smaller grains, which could be due to different nucleation and growth conditions in the early stages of film deposition. As observed in both cross-sectional and plan-view (Fig. 4c, inset) images, the film surface is rough due to the rounded tops of the columnar grains.
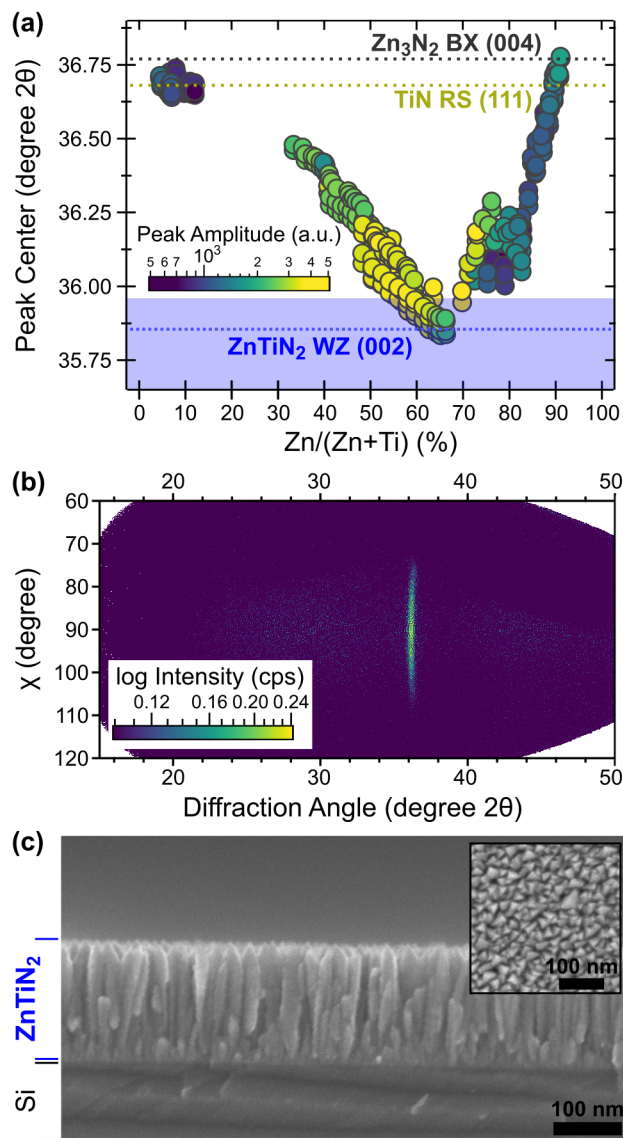
Fig. 4 Crystallinity of ZnTiN$_2$ thin films. (a) Peak position vs. composition for an exploration of deposition conditions, with peak amplitude used as a proxy for crystallinity. Peak positions are from binary nitride phases

(Zn_3N_2: ICSD #84918,[65] TiN: ICSD #656836[66]) or, for $ZnTiN_2$, highlighted as a range based on the experimental peak position shift for the (002) peak of the WZ phase in Fig. 1b. Deposition conditions for the $ZnTiN_2$ films presented here are given in Table S1. (b) Representative area detector signal (Cu Kα radiation) for optimized $ZnTiN_2$ deposition with strong (002) texturing, showing a single peak at $2\theta = 36°$ with a 40° width in χ. Grazing incidence XRD confirming the presence of wurtzite signature peaks can be seen in Fig. S2. (c) Cross-sectional SEM showing columnar grains and textured morphology with plan-view inset showing triangular cross-sections; both scale bars are 100 nm.

2.3 Optoelectronic properties of cation-disordered $ZnTiN_2$

Electronic transport measurements were carried out to determine the carrier dynamics of sputtered $ZnTiN_2$ thin films. Colinear four-point probe resistivity measurements collected on films with near-stoichiometric compositions, $0.48 < Zn/(Zn+Ti) < 0.54$, show a resistivity of ca. $\varrho = 0.3$ Ω-cm ($\sigma = 3$ S cm^{-1}) with Ti-rich concentrations having a lower resistivity (Fig. 5a), as expected with the addition of electrons into the conduction band of an already n-type material. To verify that $ZnTiN_2$ is n-type, we performed near-room-temperature Seebeck coefficient measurements and found $S = -50$ μV K^{-1} (Fig. 5b). The negative sign confirms electrons as the majority carrier and the magnitude is indicative of a highly doped semiconductor. Hall measurements from stoichiometric $ZnTiN_2$ were unsuccessful due to high resistivity, which is not unexpected. In-plane transport measurements are expected to exhibit low charge carrier mobility due to grain boundary scattering from the columnar microstructure, which is often seen in sputtered thin films (see Fig. 4c). Assuming an upper limit on carrier mobility of $\mu = 0.1$ cm^2 V^{-1} s^{-1} along with the fundamental relationship $\sigma = ne\mu$, we estimate a lower bound on the carrier density of ca. $n \approx 10^{19}$ cm^{-3}. Carrier densities of this order of magnitude are commonly observed in early-stage nitride semiconductors and arise primarily from oxygen impurities. Since O concentrations are on the several % scale (see Fig. 3a) and each O_N defect has an excess valence electron, even small dopant activation efficiencies will lead to large carrier densities.
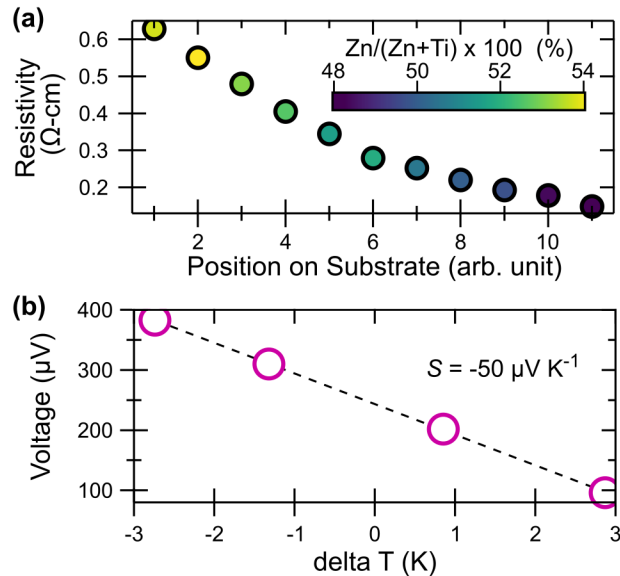

Fig. 5 Electrical properties of cation-disordered $ZnTiN_2$ (a) Resistivity across cation composition, $Zn/(Zn+Ti)$ extracted from four point probe measurements. The x axis indicates the position on the substrate and illustrates the even nature of the cation gradient across the substrate. (b) Seebeck characteristics, where the circles are measured data and the dotted line is the fit.

The optical properties of $ZnTiN_2$ thin films with $0.46 < Zn/(Zn+Ti) < 0.53$ were studied using ultraviolet-visible (UV-vis) transmission and reflection spectroscopy, as shown in Fig 6. For all compositions, a drop in the reflection-corrected transmission (Fig. 6a) is observed near 2 eV, as expected from a mid-gap semiconductor similar to other II-IV-N_2 materials[32,47] and in agreement with prior Heyd-Scuseria-Ernzerhof (HSE) calculations. Conversion to absorptivity (Fig. 6b), shows an onset in the $1.5 – 2.0$ eV range, with a slightly lower energy onset for films with high Zn concentration. While this trend may point to a degree of band gap tunability with composition, the signal may alternatively arise from a Burstein-Moss shift rather than increase in the fundamental gap as the excess electrons arising from anti-site Ti_{Zn} defects would populate the conduction band. There is less shift in the absorption curve for Zn-rich films, though alloys of ternary nitride wurtzite semiconductors and ZnO are also known to affect optical absorption properties.[67,68] In all cases, $1.5 – 2.0$ eV is significantly lower than the ~3.5 eV band gap previously predicted for $ZnTiN_2$, which is likely related to the cation disorder as observed in XRD.
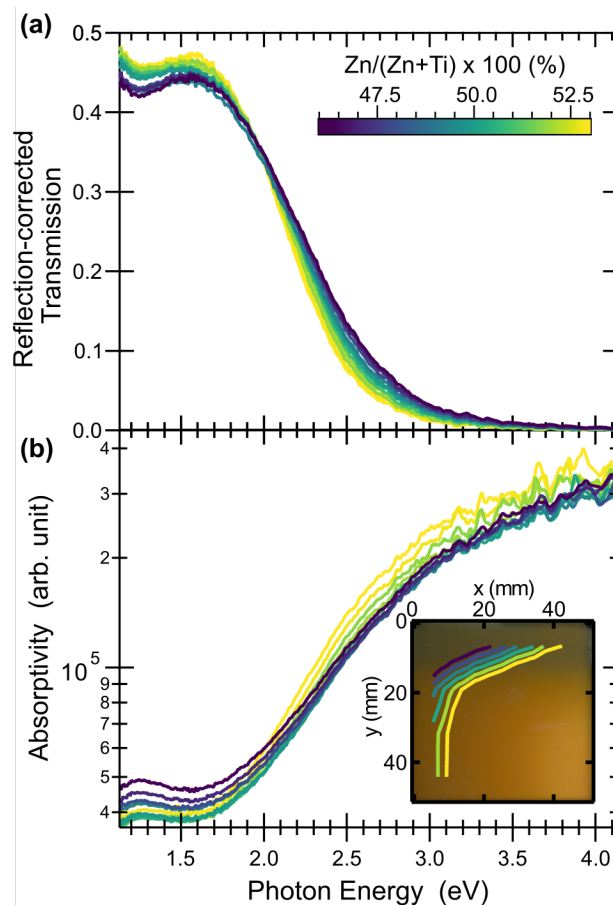

Fig. 6 Optical properties of cation-disordered $ZnTiN_2$ (a) Reflection-corrected transmission (b) Absorptivity, with the inset figure showing cation composition contours across a photograph of a $ZnTiN_2$ sample. The cation composition scalebar in (a) applies to the entire figure.

2.4 Electronic structure of $ZnTiN_2$

To understand the difference between the predicted 3.5 eV band gap of cation-ordered $ZnTiN_2$ previously reported[31] and the experimentally measured optical absorption onset reported here, we performed DFT calculations introducing specific types of cation disorder (see Methods). Cation-ordered $ZnTiN_2$ takes up an orthorhombic structure ($Pna2_1$, space group 33) containing four formula units, and can be thought of as a crystalline network of corner-sharing N-centered tetrahedra with two Zn and two Ti at the vertices, denoted as $N-Zn_2Ti_2$. DFT-PBE calculated lattice parameters are a = 5.71 Å, b = 6.59 Å, and c = 5.26 Å, slightly overestimating the experimentally-derived parameters (Section 2.1). N-cation bond lengths for the $N-Zn_2Ti_2$ motif (and for the other motifs discussed later) are shown in Table 1. Fig.7 shows the band structure of cation-ordered $ZnTiN_2$, calculated with DFT-HSE. Our computed DFT-HSE band gap is 3.36 eV, which is consistent with previous calculations[31] but overestimates our experimental measurements (our DFT-PBE band gap is significantly smaller at 2.25 eV, as expected). While DFT-PBE is expected to underestimate the band gap, DFT-HSE is known to improve accuracy of the gap for some materials.[69] Examining the projected density of states (DOS) for the cation-ordered structure, we find that the valence band edges are dominated by N p states, consistent with reports of other zinc ternary nitrides with similar structure, such as $ZnSnN_2$[31,70,71] and $ZnGeN_2$.[54,72] The conduction band edges are dominated by Ti d states, in contrast to $ZnSnN_2$ and $ZnGeN_2$ where conduction band edges are dominated by N p states.[31,70,71]

Table 1 Calculated N-cation bond lengths for the three types of tetrahedral motifs.

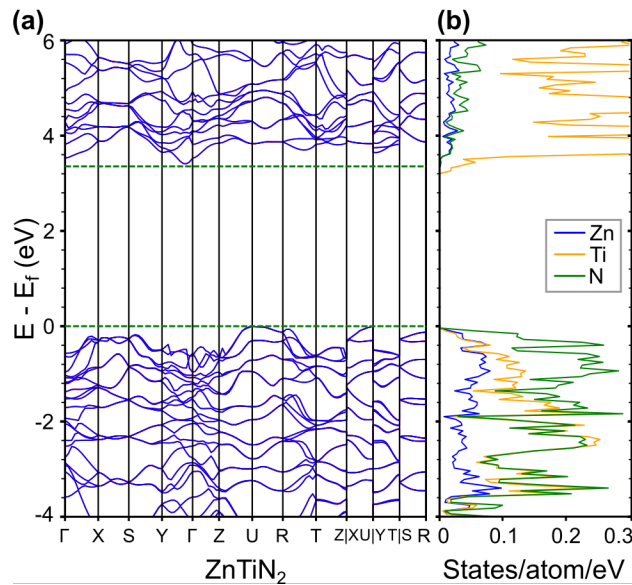|	$N-Zn_2Ti_2$	$N-Zn_1Ti_3$	$N-Zn_3Ti_1$
N-Zn bond length (Å)	2.06	2.14	2.02
N-Ti bond length (Å)	1.95	1.99	1.87

Fig.7 (a) Calculated electronic band structure with DFT-HSE of cation-ordered $ZnTiN_2$ (b) Projected DOS.

The experimentally synthesized $ZnTiN_2$ is cation-disordered by XRD; that is, the material features a high density of antisite defects, where the positions of Zn and Ti atoms are swapped relative to the cation-ordered structure (although experimental quantification of cation-site

disorder is difficult, see Ref [52]). To computationally investigate the influence of these antisite defects on the electronic structure, we construct 2×2×2 supercells containing 32 formula units (128 atoms) and introduce one or more Zn-Ti antisite defects. The primary motif of the cation-ordered structure, an N-centered Zn_2Ti_2 tetrahedron, obeys the octet rule, where each N-centered tetrahedron has exactly two Zn and two Ti atoms such at that charge neutrality is conserved locally.[73] Swapping a Zn and Ti atom in the structure introduces two types of octet-rule-violating N-centered tetrahedra, $N\text{-}Zn_1Ti_3$ and $N\text{-}Zn_3Ti_1$. We focus on three supercells in which we introduce $N\text{-}Zn_1Ti_3$ and $N\text{-}Zn_3Ti_1$ tetrahedra to investigate different examples of cation disorder. In supercell I, we swap a single Zn and Ti between distant (non-neighboring) tetrahedra; in supercell II, we swap a single Zn and Ti in one tetrahedron; in supercell III, we perform two swaps of Zn and Ti inside one N-centered tetrahedron. The numbers of octet-violating tetrahedra introduced in each supercell are shown in Table 2, and the supercells are shown in Fig. 8a, with changes to N-cation bond lengths reported in Table 1. We compute the energetic cost of creating these antisite defects to be on the order of tens of meV per formula unit, comparable to prior work on cation-disordered $ZnGeN_2$[52,72] and consistent with the observation of cation disorder in $ZnTiN_2$ deposited at ambient temperatures. We note that while the specific cation swaps considered here do not necessarily reflect the most likely atomic configurations,[70,74] they nonetheless provide insight into the impact of antisite defects on the electronic structure of $ZnTiN_2$, as we show below.

Table 2 Calculated band gaps and energy costs of $ZnTiN_2$ with different antisite types from 128-atom supercells. All tabulated band gaps and energies are computed with DFT-PBE.

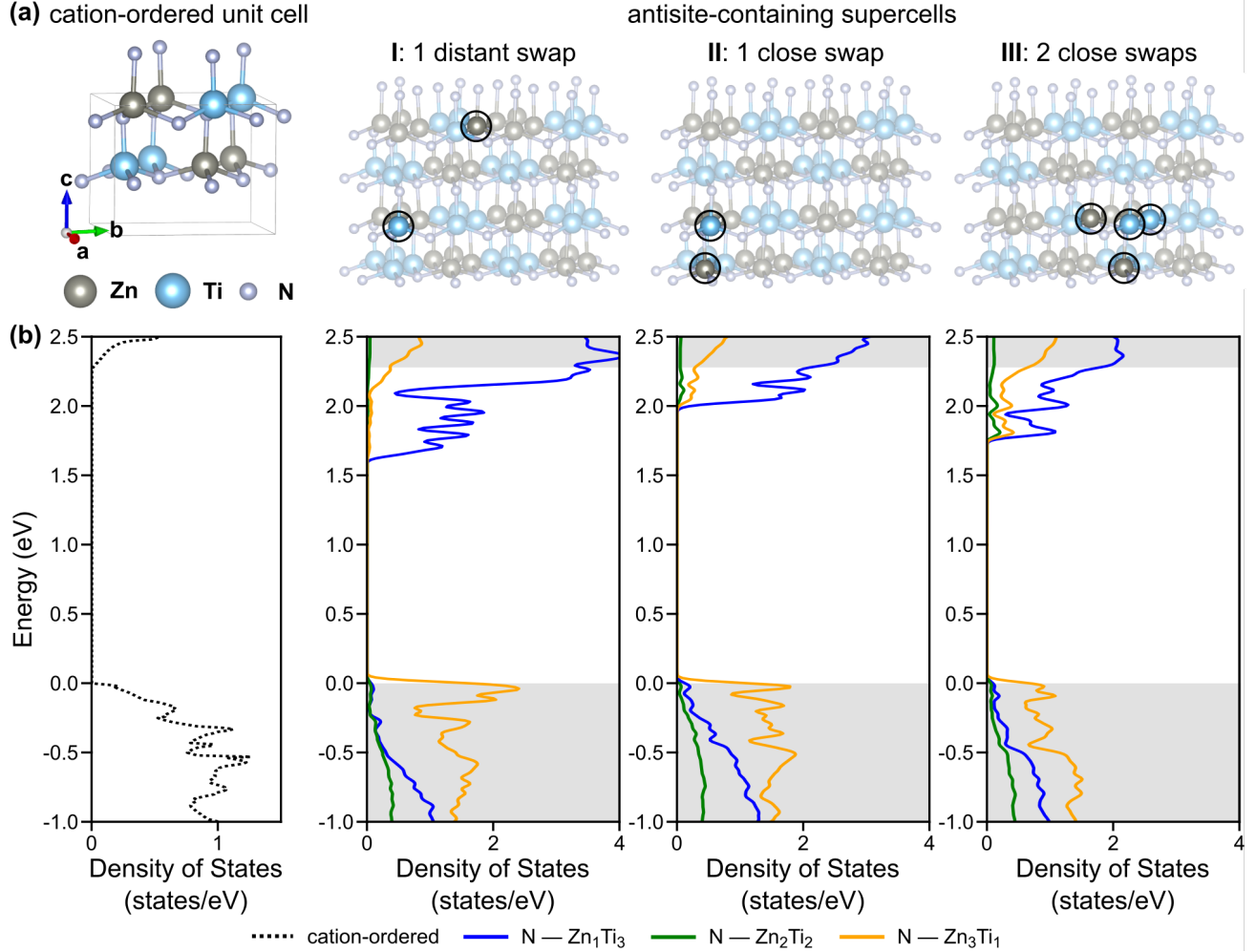|	Cation-ordered $ZnTiN_2$	I: 1 distant swap	II: 1 close swap	III: 2 close swaps
$N\text{-}Zn_1Ti_3$ motif density	0	6.25% (4/64)	4.69% (3/64)	9.38% (6/64)
$N\text{-}Zn_3Ti_1$ motif density	0	6.25%	4.69%	9.38%
band gap (eV)	2.25	1.64	2.00	1.78
relative energy per formula unit (eV)	0	0.042	0.024	0.049

Fig.8 (a) Crystal structures of cation-ordered $ZnTiN_2$ and three antisite-containing 128-atom supercells with the exchanged Zn and Ti atoms highlighted. (b) Partial density of states per N-centered tetrahedra for the cation-ordered material and the three supercells, with the contributions from the different N-centered tetrahedra illustrated. Grey shading indicates the band edges from the cation-ordered material. Gaussian smearing is used in our Brillouin zone integrations, using a smearing parameter of 0.03 eV.

Our calculations of the electronic structure of our antisite-containing supercells demonstrate that the presence of antisite defects significantly reduces the band gap relative to the cation-ordered structures for all three supercells (Table 2). The DFT-PBE band gap in supercell I is computed to be reduced by 0.61 eV and the gap in supercell II is reduced by 0.25 eV. Relative to our computed DFT-PBE gap of the cation-ordered phase of 2.25 eV, these represent significant reductions of 11% and 27%, respectively. Introducing more octet-rule-violating N-centered tetrahedra in supercell III, with two close swaps, we find that the DFT-PBE band gap of $ZnTiN_2$ is reduced by 0.47 eV (21% relative to the cation-ordered reference), intermediate between the other two supercells. The band gap reductions we computed in these three supercells are consistent with previous calculations that consider antisite defects in $ZnGeN_2$[54] and $ZnSnN_2$.[70] From these calculations, we can conclude that the band gap reduction difference is affected by *both* the number of the octet-rule-violating tetrahedra and their relative spatial separation. The smaller band gap reduction in the supercell III with 2 close swaps may result

from clustering of octet-rule-violating N-centered tetrahedra, and partial compensation by neighboring tetrahedra.

To better understand the calculated reduction in band gap with antisite defects, we examine the contributions of each of the three types of tetrahedra (N-Zn_1Ti_3, N-Zn_3Ti_1, and N-Zn_2Ti_2) to the projected partial DOS (from DFT-PBE) for each antisite-containing supercell and compare to the cation-ordered case (Fig. 8b). In all three supercells, states closer to the conduction band edges are dominated by N-Zn_1Ti_3 tetrahedra, and states closer to the valence band edges are dominated by N-Zn_3Ti_1. For N-Zn_1Ti_3, the conduction band edge states are predominately of Ti character; for N-Zn_3Ti_1, the valence band edge states are predominantly of N character. Since the corner atoms of the octet-rule-violating N-Zn_1Ti_3 tetrahedra would be more positively charged than in N-Zn_2Ti_2, intuitively the binding energy of electrons is increased relative to N-Zn_2Ti_2, introducing states below the cation-ordered conduction band edge and resulting of an overall downward shift of the N-Zn_1Ti_3 corresponding bands toward lower energies relative to the cation-ordered structure. Along the same lines, the corner atoms of N-Zn_3Ti_1 would be less positively charged, decreasing the electron binding energy and introducing states above the valence band edge, leading to an upward shift of the N-Zn_3Ti_1 corresponding bands to higher energies. In this way, the contributions to the electronic structure from both types of tetrahedra associated with cation disorder lead to an overall reduction in band gap. We note that the presence of these antisite defects not only leads to a shift in energy of the conduction and valence band edges (reducing the gap), but it also increases the localization of states in conduction band edges and valence band edges, as evidenced by the reduced band dispersion.

2.5 Electrochemical and surface properties

With an understanding of the synthesis and materials chemistry of $ZnTiN_2$, we investigate the behavior of this material under CO_2R-relevant conditions. Fig. 9a-c show selected regions of Pourbaix diagrams for $ZnTiN_2$ calculated using data from the Materials Project[60,61] at three ionic concentrations (complete diagrams are shown in Fig. S3). These diagrams are built from a combination of r^2SCAN metaGGA and PBE GGA DFT calculations using the computational Pourbaix formalism of Persson et al.[61] and the DFT mixing scheme of Kingsbury et al.[62] (see Methods). Including metaGGA calculations is beneficial because SCAN (on which r^2SCAN is based) was shown to predict ternary nitride formation enthalpies in the nitrogen-rich region of the phase diagram more accurately than GGA.[75] At the near-neutral, reducing conditions required for CO_2R, the $ZnTiN_2$ surface is expected to decompose to either TiO_2 or $Ti_3Zn_2O_8$ with or without ZnO, depending on the solution concentrations of Zn, Ti, and N. Both TiO_2[19] and ZnO[76] are established protective coatings for photoelectrodes; thus, the calculations suggest that $ZnTiN_2$ may be stabilizable as a photoabsorber for CO_2R. The Pourbaix analysis indicates that these same passivation layers may stabilize $ZnTiN_2$ under OER conditions over the entire pH range (see Fig. S3), highlighting the breadth of opportunities for its further development as a solar photocatalyst.
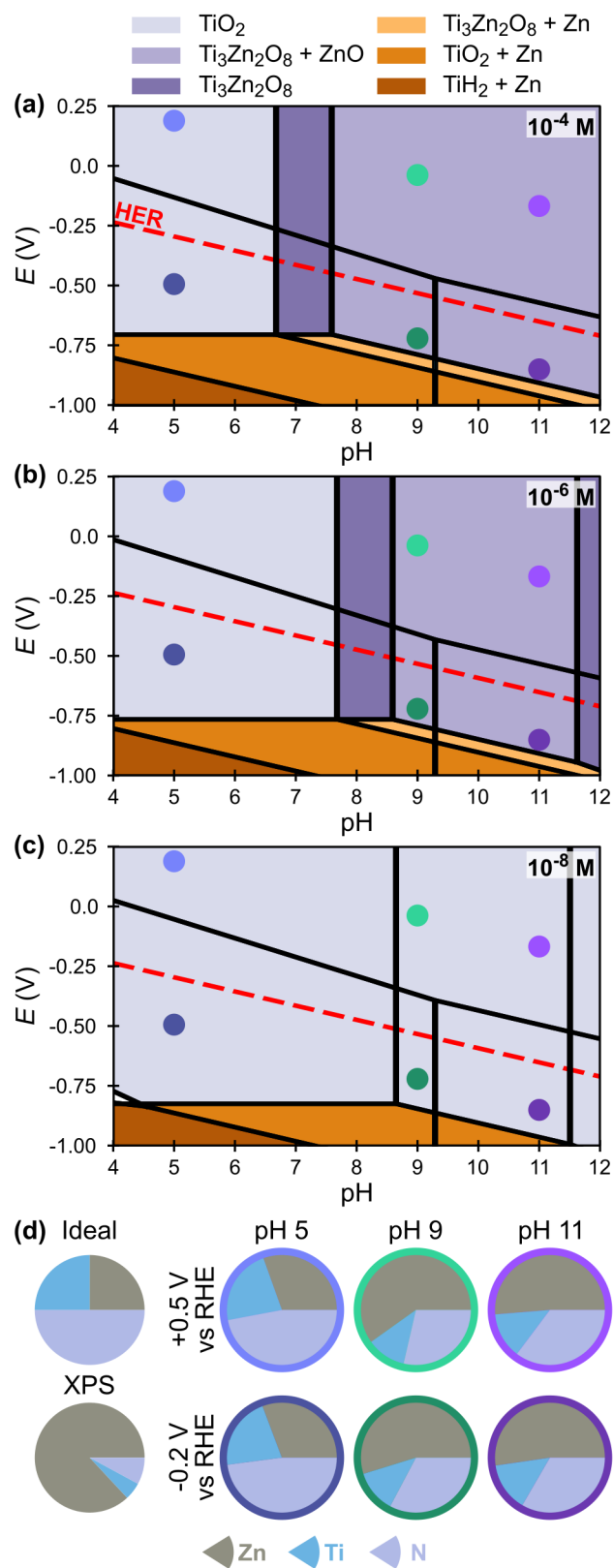
Fig. 9 (a – c) Calculated Pourbaix diagram regions for ZnTiN$_2$ at (a) 10^{-4} M, (b) 10^{-6} M, and (c) 10^{-8} M from the Materials Project, showing only stable solid phases by color (the small white region in (c) at pH 4 has no solid stable phase). No changes to the stable solid phases occur at more oxidizing potentials; see Fig. S3 for complete diagrams.

Markers in (a – c) correlate to (d), where pie charts illustrate the surface composition of the $ZnTiN_2$ films (by XPS, normalized to Zn, Ti, N) following polarization at either +0.5 V or -0.2 V vs RHE, in comparison to the ideal composition and the previously measured surface composition by XPS (Fig. 3b). Oxygen is omitted from these charts due to the convoluting presence of O-containing supporting electrolytes. Full elemental characterization of the surfaces, including residual supporting electrolyte, can be seen in Table S2. Colors surrounding the post-polarization pie charts correlate to trace colors in Fig. 10.

To further evaluate passivation of the $ZnTiN_2$, nominally cation stoichiometric $ZnTiN_2$ alloys (0.48 < Zn/(Zn+Ti) < 0.52) were electrochemically polarized in the dark. As discussed above (see Fig. 3b), XPS shows that the surface (~top 10 nm) is very Zn-rich and has oxidized substantially, with very little N present. The $ZnTiN_2$ films were polarized to either -0.2 V or +0.5 V vs the reversible hydrogen electrode (RHE) for 15 minutes at pH 5, 9, or 11. Changes to the surface compositions are shown in Fig. 9d; these changes correlate more strongly with pH than E, as surface compositions are roughly the same by pH. At pH 5, concentrations of N are near-stoichiometric (50% of the total Zn + Ti + N), while there is slightly more Zn than Ti. At pH 9 and 11, the surface is >50% Zn as in Fig 3b, but substantially more Ti and N are observed than in the XPS measurement of the unpolarized surface. Only the concentrations of Zn, Ti, and N are compared to track changes to these bulk elements at the surface. Oxygen concentrations are omitted for surface compositions of the polarized samples due to the convoluting presence of O-containing supporting electrolytes (phosphate and carbonate).[7] Full surface elemental compositions can be found in Table S2.

XPS spectra for each element across polarization conditions are compared to the representative film before polarization in Fig. 10. The Zn $2p_{3/2}$ spectra strongly indicates only one oxidation state across conditions (consistent with Zn^{2+} in both ZnO and $ZnTiN_2$).[77] In contrast, there are multiple environments for Ti^{4+}, with relative amounts changing with pH. We attribute the lower-energy peak at ~457 eV to the bulk environment of $ZnTiN_2$ and the higher-energy peak at ~458 eV to the formation of TiO_2.[78] No clear indication of TiN (~456 eV) is present, but there may be a small contribution at pH 11; at pH 5, there is a small amount of reduced Ti^0 (~454 eV). The N 1s spectra indicate N^{3-} and change only minimally with polarization at any condition, consistent with N leaving the film rather than changing oxidation state at the surface. This is in turn consistent with the Materials Project Pourbaix calculations which indicate no stable solid phases incorporating N. Finally, the O 1s spectra initially shows two distinct bonding environments, which we attribute to metal oxides (~530.5 eV) and ZnO with O vacancies (~532.5 eV),[79] consistent with the pre-polarization surface stoichiometry. After polarization, the O spectra are complicated by the retention of supporting electrolyte which contributes substantially to observed intensity. Residual phosphates at pH 5 and 11 dominate the spectra, while at pH 9 the higher energy peak can be attributed to carbonate.[80]
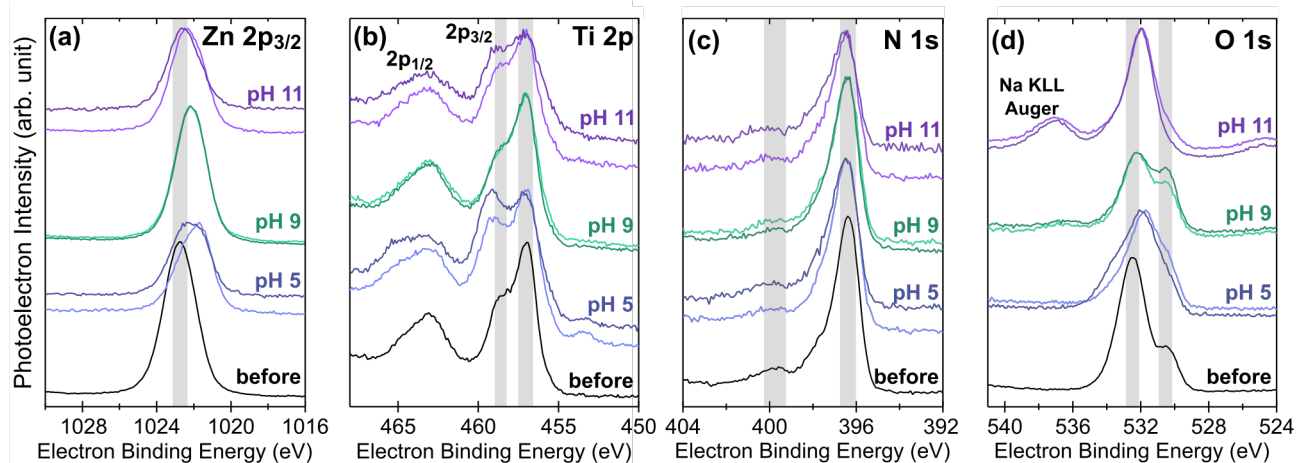
Fig. 10 XPS spectra for individual elements comparing the initial ZnTiN$_2$ surface (before) from a representative film to the results of the polarization studies (labeled with pH; darker color indicates -0.2V while lighter indicates +0.5V polarization, as in Fig.9). Grey bars are guides for the eye for indicative peaks described in the text. (a) Zn 2p$_{3/2}$ (b) Ti 2p (c) N 1s (d) O 1s.

The changes in composition and XPS spectra with polarization indicate evolution of ZnTiN$_2$ surface, although XRD collected on the films show no new crystalline phases in the bulk of the material (Fig. S4). The surface changes at pH 5 are distinct from those at pH 9 and 11, which are broadly similar. After polarization at pH 5, the surface compositions are closer to the RBS-measured bulk film composition than the pre-polarization XPS composition (see Fig. 3), although the surfaces are still enriched with Zn. The near-stoichiometric N concentration indicates that if a surface oxide is present after polarization, that oxide is not thicker than the probe depth of the XPS (~10 nm). The peak assigned to TiO$_2$ in the Ti 2p XPS spectra is enhanced in both pH 5 scans compared to the pre-polarization surface, suggesting TiO$_2$ formation. The peaks in the Zn 2p$_{3/2}$ and O 1s spectra are also shifted, which may suggest removal of the pre-polarization ZnO and, with the N concentration, exposure of ZnTiN$_2$ at the surface. This is consistent with the Materials Project Pourbaix calculations which show that ZnO should not be stable at pH 5 regardless of solution concentration, while TiO$_2$ is stable (Fig. 9a-c).

After polarizations at pH 9 and 11, there is more N present than in the pre-polarization scan (but less than at the surface at pH 5). The peaks in the Zn 2p$_{3/2}$ spectra are closely aligned with their pre-polarization position, as are the O 1s peaks at ~532.5 eV, suggesting that the pre-polarization ZnO environment has not changed dramatically. The Materials Project Pourbaix calculations indicate that the surface composition at these pH values is largely concentration dependent, with a mixed Ti$_3$Zn$_2$O$_8$ + ZnO occurring at higher concentrations and TiO$_2$ at lower concentrations (Fig. 9 a-c). The increased concentration of Ti at the surface and changes to the Ti 2p spectra at pH 11 (increase in the ~458 eV peak relative to the ~456 eV peak) may indicate the formation of some Ti-containing oxide, but because the ZnTiN$_2$ surface was initially very Zn-rich, the stoichiometric ratio of Zn:Ti cannot be used to identify the formation of the mixed oxide phase. However, these data do suggest that a thin oxide persists at the surface of the ZnTiN$_2$ film at alkaline pH. With the data indicating TiO$_2$ formation at the surface at pH 5, these are promising indicators for further investigation of ZnTiN$_2$ as a CO$_2$R or OER photoelectrode across aqueous environments.

3. Summary and Conclusions

Herein we envision a new generation of photocatalysts discovered through co-design for operational stability and facile integration into high-efficiency devices. We report the first photocatalyst identified via this co-design approach, $ZnTiN_2$. We investigate the crystal structure and physical properties of $ZnTiN_2$ synthesized by reactive sputtering from metallic Zn and Ti precursors in a N_2 atmosphere. We investigate the surface chemistry of these thin films under electrochemical l conditions to evaluate them for potential (photo)electrochemical applications, such as in CO_2R and OER. Overall, the newly synthesized $ZnTiN_2$ wurtzite semiconductor may have bulk optoelectronic properties and self-passivating surface chemistry suitable for photoelectrochemical fuel generation.

The sputtered $ZnTiN_2$ thin films with columnar microstructure form in a cation-disordered wurtzite-derived crystal structure with strong (002) preferential orientation, in a relatively broad range Zn-rich compositions limited by the formation of rocksalt TiN and anti-bixbyite Zn_3N_2. Chemical composition measurements indicate unintentional oxygen incorporation of less than 10% of the anion content in the bulk of the layers, with self-passivating zinc-based native oxide formation at the film surface. The $ZnTiN_2$ films show 0.3 Ω-cm electrical resistivity and $S = -50\mu V\ K^{-1}$ Seebeck coefficient, indicating n-type conduction and suggesting high electron doping. The measured optical absorption onset of these cation-disordered films is close to 2 eV, which is significantly lower than the theoretical 3.5 eV theoretical band gap for cation-ordered $ZnTiN_2$ determined by N 2p derived valence band maximum and Ti 3d derived conduction band minimum. Theoretical calculations reported here show that the difference is attributable to band gap narrowing due to upward shift of the valence band caused by N-centered Zn_3Ti_1 tetrahedral motifs, and downward conduction band shift caused by the $N-Zn_1Ti_3$ motifs in cation-disordered $ZnTiN_2$. XPS measurements indicate that the $ZnTiN_2$ photoelectrode surfaces exposed to high pH (9, 11) have ZnO-like character, whereas the pH 5 treated surfaces show some TiO_2-like character as well as exposed $ZnTiN_2$, regardless of the applied potential in the studied range.

To realize the full potential of $ZnTiN_2$ as a semiconductor for photoelectrochemical applications, it would be important to improve its charge transport properties by growing high-quality thin films on lattice-matched substrates. Epitaxial growth on p-type GaN would be particularly promising for improving the photoexcited hole extraction from n-type $ZnTiN_2$ absorber. Another critical step will be to evaluate potential epitaxial relations of $ZnTiN_2$ with the ZnO and TiO_2 decomposition products, and study band alignment for charge transport between this absorber and its self-passivating surface coatings. The results reported in this paper, as well as the future research directions discussed here, illustrate a new materials design strategy to develop photoelectrochemically active semiconductors with native operational surface chemistry tuned for durability under their operating conditions.

4. Methods

4.1. Synthesis

Initial polycrystalline Zn-Ti-N films were deposited by co-sputtering from Zn and Ti targets in N plasma on stationary (001)-oriented Si substrates without intentional heating, in a custom vacuum chamber with base pressure of $<10^{-7}$ Torr enhanced by a cryoshroud surrounding the plasma zone. The 2" diameter targets were pointed at an angle at the substrate and were excited by radio-frequency (RF) field of Zn = 13 W and Ti = 60 W. The N plasma intensity was

enhanced by RF plasma source at 350 W. The deposition pressure was set to 6 mTorr by flowing 3 sccm of N_2 and 6 sccm of Ar through a partially closed gate valve. The 1-hour deposition led to a 50 nm thick Zn-Ti-N film, with a gradient of cation composition across the sample resulting from stationary substrate and angled targets during the deposition. Before and after the Zn-Ti-N deposition, 40 nm thick AlN layers were deposited by sputtering from a metallic Al target at 60W onto a rotating substrate under the same conditions to enhance polycrystallinity of the resulting material for structure identification, and to suppress Zn volatilization during annealing. These samples were subject to rapid thermal annealing (RTA) in flowing N_2 atmosphere at ambient pressure for 3 min in T = 500 °C – 700 °C temperature range, following a 3 min hold at 100 °C to drive off water.

Optimization of Zn-Ti-N film crystallinity was performed in a second custom vacuum chamber, with base pressure of $<10^{-7}$ Torr enhanced by a cryoshroud surrounding the plasma zone. Highly textured Zn-Ti-N films were deposited by co-sputtering from 2" Zn and Ti targets in a N and Ar plasma onto stationary Corning® EXG glass substrates; the targets were positioned 180 degrees from one another and pointed at an angle towards the substrate, creating a composition gradient in the deposited film. Target powers were varied between Zn = 10 to 25 W and Ti = 100 to 150 W to tune the range of the composition gradient. The deposition pressure was either 6 mTorr or 3.5 mTorr with flows of 50 sccm of N_2 and 100 sccm of Ar. A calibrated temperature gradient was introduced perpendicular to the composition gradient by heating one end of the substrate and allowing the thermal diffusivity of the EXG glass to create a gradient in temperature (see SI). Using the knowledge gained from optimizing crystallinity, some highly-textured, near-stoichiometric films were deposited at ambient temperature onto p-type single crystal silicon or EXG glass substrates by co-sputtering from Ti (100 W) and ZnTi alloy (150 W) 2" targets for specific use in electrical, optical, microscopy characterizations as well as electrochemical studies. All depositions were conducted for 2 hours following substrate temperature stabilization and 30 minutes of pre-sputtering with the substrate covered by a shutter.

4.2 Characterization

Cation composition, reported as the ratio of Zn/(Zn+Ti), was measured by collecting and analyzing X-ray fluorescence spectra (XRF) with a Fischer XDV-SDD and the accompanying analysis software. X-ray diffraction (XRD) was acquired over a range of 2θ = 19° to 52° and χ = 60° to 120° using a Bruker D8 Discover equipped with an area detector. Scanning electron microscopy was performed using a Hitachi S-4800 operating at 3 kV accelerating voltage, 5 μA emission current, and a working distance of 3.5 mm. Rutherford backscattering spectrometry (RBS) data were acquired using a Model 3S-MR10 RBS system from National Electrostatics Corporation. The RBS measurements were performed using 2 MeV alpha particles in a 168° backscatter configuration for a total accumulated charge of 80 μC, and compositions were determined by modeling the spectra using RUMP software using the simplest possible two-layer (substrate + film) model.[81] Anion concentrations were visually overfit by the software's built in least squares algorithm, likely related to a weak signal for low-Z elements on top of a large substrate background. Instead, we modeled various fixed anion combinations and found a good qualitative match when [N]+[O] = 2 (i.e., equal to [Zn]+[Ti] for stoichiometric compositions) and [O]/([O]+[N]) = 0.1.

Optical data were collected on a custom-built UV-vis transmission and reflection optical spectroscopy instrument equipped with halogen and deuterium lamps. The transmission and

reflection spectra were used to calculate absorptivity, $\alpha = -\ln[T/(1-R)]/t$, where t is the thickness as measured by stylus profilometry (Dektak). The as-measured high α values (ca. 10^5 cm^{-1}) are likely due to unaccounted diffuse reflectance or other optical losses, so α values are reported in arbitrary units. Library photographs were collected using a color-calibrated desktop scanner in transmission mode.

      Resistivity data were collected on a colinear four-point probe instrument by sweeping current between the outer two pins while measuring voltage between the inner pins. Conventional geometric corrections were applied to convert the measured resistance into sheet resistance and then resistivity. Seebeck coefficients were measured on a lab-built instrument. Here, the sample is suspended across two thermally and electrically isolated copper blocks, each fitted with cartridge heaters and embedded copper-constantan thermocouples, with contacts made by pressed indium dots. One block is heated to slightly above room temperature while the temperature of each is monitored by the thermocouples and the thermovoltage is measured by the like-metal thermocouple leads across two blocks. This is repeated to create a dV/dT curve, the slope of which is then corrected for the instrument's calibrated Seebeck coefficient to determine the sample Seebeck coefficient. Mapping data (XRD, XRF, UV-vis, and four-point probe) were analyzed using CombIgor, a custom *Igor Pro* (WaveMetrics, Lake Oswego, OR, U.S.A.) add-on.[82] Data was harvested and processed using NREL's Research Data Infrastrcture[83] and will be made available through the High Throughput Experimental Materials Database.[84]

      Electrochemical polarization experiments used ZnTiN$_2$ films deposited on conductive Si with $0.48 < $ Zn/(Zn+Ti) $ < 0.52$. XPS data for the as-grown samples were obtained on an Omicron XPS setup and were consistent across the composition range. Films were fabricated into electrodes using electrodeposition tape and acted as working electrodes with a Pt counter electrode and saturated calomel reference electrode. Electrolytes were buffered to the correct pH (5, 9, or 11) using Hydrion buffers. ZnTiN$_2$ electrodes were polarized using a BioLogic SP-300 at either -0.2 V or +0.5 V vs RHE (corrected for pH) for 15 minutes. Post electrochemical polarization, XPS data were obtained on a Physical Electronics Versa Probe III using Al Kα radiation. For both pre- and post-polarization XPS measurements, the XPS setup was calibrated with Au and/or Cu metal, which was cleaned via Ar-ion sputtering. The raw atomic concentration has a 5% error due to surface inhomogeneities, surface roughness, literature sensitivity values for peak integration, *etc*.

4.3 Calculations

      Our density functional theory (DFT) calculations within the generalized gradient approximation (GGA) are performed with the Vienna Ab Initio Simulation Package (VASP).[85,86] We use the exchange-correlation functional of Perdew, Burke, and Ernzerhof (PBE)[87] to relax structures and compute electronic structures. In certain cases, we also use the Heyd-Scuseria-Ernzerhof (HSE06) screened hybrid functional[88,89] to compute electronic structure. An energy cutoff of 600 eV is used for all calculations. Total energies are converged to within 10^{-5} eV and all Hellmann-Feynman forces are below 0.01 eV/Å on each atom. For all calculations, we use the projector augmented wave potentials, treating 3d2 4s2, 3d10 4s2, and 2s2 2p3 electrons explicitly for Ti, Zn, and N, respectively. We consider cation ordered and disordered structures. The cation-ordered orthorhombic structure (16 atoms) has a *Pna*2$_1$ space group and contains 4 formula units (f.u.). Our cation-disordered structure (128 atoms) is based on a 2×2×2 supercell of the cation-ordered structure but includes selected antisite defects. A Γ-centered 10×10×8 Monkhorst-Pack k-mesh is used for calculations involving the 4 f.u. cation ordered unit cell; and

a 4×4×4 k-mesh is used in 16 f.u. supercell. Gaussian smearing is used in our Brillouin zone integrations, using a smearing parameter of 0.02 eV in structure relaxation and 0.03 eV in static density of states calculation. The N-Ti or N-Zn bond length in octet-rule-violating N-centered tetrahedra motif in Table 1 are the averaged bond lengths in each cation-disordered supercell structure, which is the same within 0.01 Å among three supercells, while N-Ti or N-Zn bond length in N-Zn_2Ti_2 is the averaged bond length in cation-ordered structure.

Our electrochemical stability calculations (Pourbaix diagrams) are built from a combination of PBE GGA DFT calculations retrieved from the Materials Project database and regulated-restored strongly-constrained and appropriately normed (r²SCAN) metaGGA calculations calculated using the workflow detailed in Kingsbury et al.[90] We used the Materials Project DFT mixing scheme[62] to combine these two sets of calculations and create a solid phase diagram of the Zn-N-Ti-O-H chemical system, from which we constructed Pourbaix diagrams using the computational formalism of Persson et al.[61] The mixing scheme allowed us to build the convex energy hull from higher-level metaGGA calculations by recomputing only the stable phases and phases close to the hull with r²SCAN (170 calculations total) instead of the entire Zn-N-Ti-O-H chemical system (more than 500 total phases according to the Materials Project Database). For two stable phases where the large number of sites made r²SCAN structure optimizations impractical (Ti_3Zn_{22} and $Ti_{20}H_2N_{17}$, with 100 and 39 sites, respectively) we employed single point calculations, as suggested in Kingsbury et al.[62] The stability predictions of this mixed Pourbaix diagram were qualitatively similar to those obtained from a pure GGA phase diagram constructed without any r²SCAN calculations, but predicted a slightly larger region of decomposition to $Ti_3Zn_2O_8$ and/or ZnO (see Figure S3).

5. Acknowledgements and Author Contributions

6. References

1   J. A. Gauthier, J. H. Stenlid, F. Abild-Pedersen, M. Head-Gordon and A. T. Bell, *ACS Energy Lett.*, 2021, **6**, 3252–3260.

2   M. Lin, I. A. Digdaya and C. Xiang, *Sustain. Energy Fuels*, 2021, **5**, 2149–2158.

3   C. J. Kong, E. L. Warren, A. L. Greenaway, R. R. Prabhakar, A. C. Tamboli and J. W. Ager, *Sustain. Energy Fuels*, 2021, **5**, 6361–6371.

4   C. Kim, J. C. Bui, X. Luo, J. K. Cooper, A. Kusoglu, A. Z. Weber and A. T. Bell, *Nat. Energy*, 2021, **6**, 1026–1034.

5   A. J. Welch, I. A. Digdaya, R. Kent, P. Ghougassian, H. A. Atwater and C. Xiang, *ACS Energy Lett.*, 2021, **6**, 1540–1549.

6   A. K. Singh, J. H. Montoya, J. M. Gregoire and K. A. Persson, *Nat. Commun.*, 2019, **10**, 443.

7   A. K. Singh, L. Zhou, A. Shinde, S. K. Suram, J. H. Montoya, D. Winston, J. M. Gregoire and K. A. Persson, *Chem. Mater.*, 2017, **29**, 10159–10167.

8   J. Feng, H. Huang, S. Yan, W. Luo, T. Yu, Z. Li and Z. Zou, *Nano Today*, 2020, **30**, 100830.

9   Y. Wu, P. Lazic, G. Hautier, K. Persson and G. Ceder, *Energy Environ. Sci.*, 2013, **6**, 157–168.

10 I. E. Castelli, T. Olsen, S. Datta, D. D. Landis, S. Dahl, K. S. Thygesen and K. W. Jacobsen, *Energy Environ. Sci.*, 2012, **5**, 5814–5819.

11 L. Zhou, A. Shinde, D. Guevarra, J. A. Haber, K. A. Persson, J. B. Neaton and J. M. Gregoire, *ACS Energy Lett.*, 2020, **5**, 1413–1421.

12 M. Garcia-Sanz, *Adv. Control Appl.*, 2019, **1**, e18.

13 W. Jiang, J. Xiong and Y. Shi, *Nat. Commun.*, 2021, **12**, 579.

14 K. K. Rao, Y. Lai, L. Zhou, J. A. Haber, M. Bajdich and J. M. Gregoire, *Chem. Mater.*, 2022, **34**, 899–910.

15 M. G. Kast, L. J. Enman, N. J. Gurnon, A. Nadarajah and S. W. Boettcher, *ACS Appl. Mater. Interfaces*, 2014, **6**, 22830–22837.

16 M. Ben-Naim, R. J. Britto, C. W. Aldridge, R. Mow, M. A. Steiner, A. C. Nielander, L. A. King, D. J. Friedman, T. G. Deutsch, J. L. Young and T. F. Jaramillo, *ACS Energy Lett.*, 2020, **5**, 2631–2640.

17 Z. Ye, Z. Hu, L. Yang and X. Xiao, *Sol. RRL*, 2020, **4**, 1900567.

18 R. Liu, Z. Zheng, J. Spurgeon and X. Yang, *Energy Env. Sci*, 2014, **7**, 2504–2517.

19 S. Hu, M. R. Shaner, J. A. Beardslee, M. Lichterman, B. S. Brunschwig and N. S. Lewis, *Science*, 2014, **344**, 1005–1009.

20 G. Liu, P. Fu, L. Zhou, P. Yan, C. Ding, J. Shi and C. Li, *Chem. – Eur. J.*, 2015, **21**, 9624–9628.

21 Y. Park, K. J. McDonald and K.-S. Choi, *Chem. Soc. Rev.*, 2013, **42**, 2321–2337.

22 F. F. Abdi, L. Han, A. H. M. Smets, M. Zeman, B. Dam and R. van de Krol, *Nat. Commun.*, 2013, **4**, 2195.

23 L. Zhou, Q. Yan, J. Yu, R. J. R. Jones, N. Becerra-Stasiewicz, S. K. Suram, A. Shinde, D. Guevarra, J. B. Neaton, K. A. Persson and J. M. Gregoire, *Phys. Chem. Chem. Phys.*, 2016, **18**, 9349–9352.

24 E. Nurlaela, A. Ziani and K. Takanabe, *Mater. Renew. Sustain. Energy*, 2016, **5**, 18.

25 Y. He, R. Chen, W. Fa, B. Zhang and D. Wang, *J. Chem. Phys.*, 2019, **151**, 130902.

26 I. Narkeviciute and T. F. Jaramillo, *Sol. RRL*, 2017, **1**, 1700121.

27 A. D. DeAngelis, K. C. Kemp, N. Gaillard and K. S. Kim, *ACS Appl. Mater. Interfaces*, 2016, **8**, 8445–8451.

28 Y.-C. Wang, Y.-Y. Zeng, L.-H. Li, C. Qin, Y.-W. Wang, Z.-R. Lou, F.-Y. Liu, Z.-Z. Ye and L.-P. Zhu, *ACS Appl. Energy Mater.*, 2020, **3**, 6188–6194.

29 R. R. Prabhakar, T. Moehl, S. Siol, J. Suh and S. D. Tilley, *Chem. Mater.*, 2020, **32**, 7247–7253.

30 W. Sun, C. J. Bartel, E. Arca, S. R. Bauers, B. Matthews, B. Orvañanos, B.-R. Chen, M. F. Toney, L. T. Schelhas, W. Tumas, J. Tate, A. Zakutayev, S. Lany, A. M. Holder and G. Ceder, *Nat. Mater.*, 2019, **18**, 732–739.

31 Y. Hinuma, T. Hatakeyama, Y. Kumagai, L. A. Burton, H. Sato, Y. Muraba, S. Iimura, H. Hiramatsu, I. Tanaka, H. Hosono and F. Oba, *Nat. Commun.*, 2016, **7**, 11962.

32 A. L. Greenaway, C. L. Melamed, M. B. Tellekamp, R. Woods-Robinson, E. S. Toberer, J. R. Neilson and A. C. Tamboli, *Annu. Rev. Mater. Res.*, 2021, **51**, 591–618.

33 A. Zakutayev, S. R. Bauers and S. Lany, *Chem. Mater.*, 2022, **34**, 1418–1438.

34 S. Zhuk, A. A. Kistanov, S. C. Boehme, N. Ott, F. La Mattina, M. Stiefel, M. V. Kovalenko and S. Siol, *Chem. Mater.*, 2021, **33**, 9306–9316.

35 A. L. Greenaway, A. L. Loutris, K. N. Heinselman, C. L. Melamed, R. R. Schnepf, M. B. Tellekamp, R. Woods-Robinson, R. Sherbondy, D. Bardgett, S. Bauers, A. Zakutayev, S. T. Christensen, S. Lany and A. C. Tamboli, *J. Am. Chem. Soc.*, 2020, **142**, 8421–8430.

36 N. Yamada, K. Matsuura, M. Imura, H. Murata and F. Kawamura, *ACS Appl. Electron. Mater.*, 2021, **3**, 1341–1349.

37 A. Zakutayev, *J. Phys. Condens. Matter*, 2021, **33**, 354003.

38 E. Arca, S. Lany, J. D. Perkins, C. Bartel, J. Mangum, W. Sun, A. Holder, G. Ceder, B. Gorman, G. Teeter, W. Tumas and A. Zakutayev, *J. Am. Chem. Soc.*, 2018, **140**, 4293–4301.

39 E. Arca, J. D. Perkins, S. Lany, A. Mis, B.-R. Chen, P. Dippo, J. L. Partridge, W. Sun, A. Holder, A. C. Tamboli, M. F. F. Toney, L. T. Schelhas, G. Ceder, W. Tumas, G. Teeter and A. Zakutayev, *Mater. Horiz.*, 2019, **6**, 1669–1674.

40 K. N. Heinselman, S. Lany, J. D. Perkins, K. R. Talley and A. Zakutayev, *Chem. Mater.*, 2019, **31**, 8717–8724.

41 M. F. Al Fattah, M. R. Amin, M. Mallmann, S. Kasap, W. Schnick and A. Moewes, *J. Phys. Condens. Matter*, 2020, **32**, 405504.

42 M. Mallmann, C. Maak, R. Niklaus and W. Schnick, *Chem. – Eur. J.*, 2018, **24**, 13963–13970.

43 I. S. Khan, K. N. Heinselman and A. Zakutayev, *J. Phys. Energy*, 2020, **2**, 032007.

44 A. N. Fioretti, A. Zakutayev, H. Moutinho, C. Melamed, J. D. Perkins, A. G. Norman, M. Al-Jassim, E. S. Toberer and A. C. Tamboli, *J. Mater. Chem. C*, 2015, **3**, 11017–11028.

45 A. D. Martinez, A. N. Fioretti, E. S. Toberer and A. C. Tamboli, *J. Mater. Chem. A*, 2017, **5**, 11418–11435.

46 E. W. Blanton, K. He, J. Shan and K. Kash, *J. Cryst. Growth*, 2017, **461**, 38–45.

47 C. L. Melamed, J. Pan, A. Mis, K. Heinselman, R. R. Schnepf, R. Woods-Robinson, J. J. Cordell, S. Lany, E. S. Toberer and A. C. Tamboli, *J. Mater. Chem. C*, 2020, **8**, 8736–8746.

48 S. R. Bauers, A. Holder, W. Sun, C. L. Melamed, R. Woods-Robinson, J. Mangum, J. Perkins, W. Tumas, B. Gorman, A. Tamboli, G. Ceder, S. Lany and A. Zakutayev, *Proc. Natl. Acad. Sci.*, 2019, **116**, 14829–14834.

49 C. L. Rom, M. J. Fallon, A. Wustrow, A. L. Prieto and J. R. Neilson, *Chem. Mater.*, 2021, **33**, 5345–5354.

50 J. Kim, S. R. Bauers, I. S. Khan, J. D. Perkins, B.-I. Park, K. R. Talley, D. Kim, A. Zakutayev and B. Shin, *J. Mater. Chem. A*, 2020, **8**, 9364–9372.

51 S. R. Bauers, D. M. Hamann, A. Patterson, J. D. Perkins, K. R. Talley and A. Zakutayev, *Jpn. J. Appl. Phys.*, 2019, **58**, SC1015.

52 R. R. Schnepf, J. J. Cordell, M. B. Tellekamp, C. L. Melamed, A. L. Greenaway, A. Mis, G. L. Brennecka, S. Christensen, G. J. Tucker, E. S. Toberer, S. Lany and A. C. Tamboli, *ACS Energy Lett.*, 2020, **5**, 2027–2041.

53 M. S. Haseman, M. R. Karim, D. Ramdin, B. A. Noesges, E. Feinberg, B. H. D. Jayatunga, W. R. L. Lambrecht, M. Zhu, J. Hwang, K. Kash, H. Zhao and L. J. Brillson, *J. Appl. Phys.*, 2020, **127**, 135703.

54 J. J. Cordell, G. J. Tucker, A. Tamboli and S. Lany, *APL Mater.*, 2022, **10**, 011112.

55 K. Maeda, Y. Lee, X. Wang and K. Domen, *ECS Trans.*, 2008, **13**, 135–141.

56 D. Fang and Y. Li, *Phys. Lett. A*, 2020, **384**, 126670.

57 G. Zeng, T. A. Pham, S. Vanka, G. Liu, C. Song, J. K. Cooper, Z. Mi, T. Ogitsu and F. M. Toma, *Nat. Mater.*, 2021, **20**, 1130–1135.

58 S. Vanka, K. Sun, G. Zeng, T. A. Pham, F. M. Toma, T. Ogitsu and Z. Mi, *J. Mater. Chem. A*, 2019, **7**, 27612–27619.

59 C. Tholander, C. B. A. Andersson, R. Armiento, F. Tasnádi and B. Alling, *J. Appl. Phys.*, 2016, **120**, 225102.

60 A. Jain, S. P. Ong, G. Hautier, W. Chen, W. D. Richards, S. Dacek, S. Cholia, D. Gunter, D. Skinner, G. Ceder and K. A. Persson, *APL Mater.*, 2013, **1**, 011002.

61 K. A. Persson, B. Waldwick, P. Lazic and G. Ceder, *Phys. Rev. B*, 2012, **85**, 235438.

62 R. Kingsbury, A. S. Rosen, A. S. Gupta, J. Munro, S. P. Ong, A. Jain, S. Dwaraknath, M. K. Horton and K. A. Persson, , DOI:10.26434/chemrxiv-2022-3ptwx.

63 R. Woods-Robinson, V. Stevanović, S. Lany, K. N. Heinselman, K. A. Persson and A. Zakutayev, *ArXiv201212455 Cond-Mat*.

64 V. Stevanović, S. Lany, X. Zhang and A. Zunger, *Phys. Rev. B*, 2012, **85**, 115104.

65 D. E. Partin, D. J. Williams and M. O'Keeffe, *J. Solid State Chem.*, 1997, **132**, 56–59.

66 W. Lengauer, *J. Alloys Compd.*, 1992, **186**, 293–307.

67 J. Pan, J. Cordell, G. J. Tucker, A. C. Tamboli, A. Zakutayev and S. Lany, *Adv. Mater.*, 2019, **31**, 1807406.

68 C. L. Melamed, M. B. Tellekamp, J. S. Mangum, J. D. Perkins, P. Dippo, E. S. Toberer and A. C. Tamboli, *Phys. Rev. Mater.*, 2019, **3**, 051602.

69 P. Borlido, J. Schmidt, A. W. Huran, F. Tran, M. A. L. Marques and S. Botti, *Npj Comput. Mater.*, 2020, **6**, 96.

70 S. Lany, A. N. Fioretti, P. P. Zawadzki, L. T. Schelhas, E. S. Toberer, A. Zakutayev and A. C. Tamboli, *Phys. Rev. Mater.*, 2017, **1**, 035401.

71 S. Chen, P. Narang, H. A. Atwater and L.-W. Wang, *Adv. Mater.*, 2014, **26**, 311–315.

72 D. Skachkov, P. C. Quayle, K. Kash and W. R. L. Lambrecht, *Phys. Rev. B*, 2016, **94**, 205201.

73 P. C. Quayle, E. W. Blanton, A. Punya, G. T. Junno, K. He, L. Han, H. Zhao, J. Shan, W. R. L. Lambrecht and K. Kash, *Phys. Rev. B*, 2015, **91**, 205207.

74 J. J. Cordell, J. Pan, A. C. Tamboli, G. J. Tucker and S. Lany, *Phys. Rev. Mater.*, 2021, **5**, 024604.

75 W. Sun, A. Holder, B. Orvañanos, E. Arca, A. Zakutayev, S. Lany and G. Ceder, *Chem. Mater.*, 2017, **29**, 6936–6946.

76 U. Shaislamov, K. Krishnamoorthy, S. Jae Kim, W. Chun and H.-J. Lee, *RSC Adv.*, 2016, **6**, 103049–103056.

77 B. He, Y. Yuan, J. Wang, E. Pervaiz, X. Dong, Z. Shao and M. Yang, *Electrocatalysis*, 2018, **9**, 452–458.

78 U. Diebold and T. E. Madey, *Surf. Sci. Spectra*, 1996, **4**, 227–231.

79 P. K. Nayak, Z. Wang, D. H. Anjum, M. N. Hedhili and H. N. Alshareef, *Appl. Phys. Lett.*, 2015, **106**, 103505.

80 J. F. Moulder, W. F. Stickle, P. E. Sobol and K. D. Bomben, *Handbook of X-Ray Photoelectron Spectroscopy: A Reference Book of Standard Spectra for Identification and Interpretation of XPS Data*, Perkin-Elmer Corp., 1992.

81 N. P. Barradas, K. Arstila, G. Battistig, M. Bianconi, N. Dytlewski, C. Jeynes, E. Kótai, G. Lulli, M. Mayer, E. Rauhala, E. Szilágyi and M. Thompson, *Nucl. Instrum. Methods Phys. Res. Sect. B Beam Interact. Mater. At.*, 2008, **266**, 1338–1342.

82 K. R. Talley, S. R. Bauers, C. L. Melamed, M. C. Papac, K. N. Heinselman, I. Khan, D. M. Roberts, V. Jacobson, A. Mis, G. L. Brennecka, J. D. Perkins and A. Zakutayev, *ACS Comb. Sci.*, 2019, **21**, 537–547.

83 K. R. Talley, R. White, N. Wunder, M. Eash, M. Schwarting, D. Evenson, J. D. Perkins, W. Tumas, K. Munch, C. Phillips and A. Zakutayev, *Patterns*, 2021, **2**, 100373.

84 An open experimental database for exploring inorganic materials | Scientific Data, https://www.nature.com/articles/sdata201853, (accessed 10 March 2022).

85 G. Kresse and J. Furthmüller, *Phys. Rev. B*, 1996, **54**, 11169–11186.

86 P. E. Blöchl, *Phys. Rev. B*, 1994, **50**, 17953–17979.

87 J. P. Perdew, K. Burke and M. Ernzerhof, *Phys. Rev. Lett.*, 1996, **77**, 3865–3868.

88 J. Heyd, G. E. Scuseria and M. Ernzerhof, *J. Chem. Phys.*, 2003, **118**, 8207–8215.

89 A. V. Krukau, O. A. Vydrov, A. F. Izmaylov and G. E. Scuseria, *J. Chem. Phys.*, 2006, **125**, 224106.

90 R. Kingsbury, A. S. Gupta, C. J. Bartel, J. M. Munro, S. Dwaraknath, M. Horton and K. A. Persson, *Phys. Rev. Mater.*, 2022, **6**, 013801.